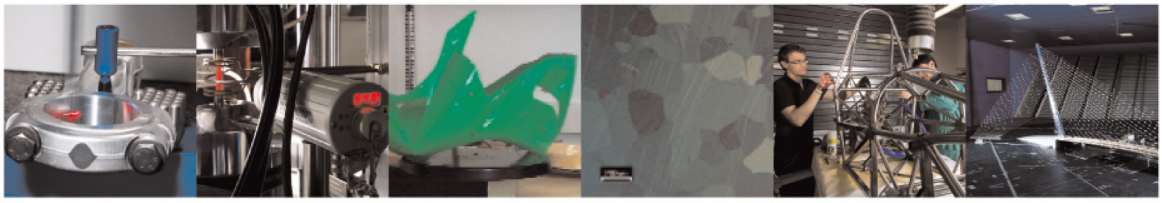

Fatigue crack growth analysis in composite bonded joints by back face distributed strain sensing and comparison with X-ray microtomography

A. Bernasconi, L.M. Martulli, M. Carboni

This is a post-peer-review, pre-copyedit version of an article published in International Journal of Fatigue. The final authenticated version is available online at:
https://doi.org/10.1016/j.ijfatigue.2021.106526

DIPARTIMENTO DI MECCANICA ■ POLITECNICO DI MILANO
via G. La Masa, 1 ■ 20156 Milano ■ EMAIL (PEC): pecmecc@cert.polimi.it
http://www.mecc.polimi.it
Rev. 0

Fatigue crack growth analysis in composite bonded joints by back face distributed strain sensing and comparison with X-ray microtomography

A. Bernasconi[1*], L.M. Martulli[1], M. Carboni[1]

[1]Department of Mechanical Engineering, Politecnico di Milano, Via La Masa 1, 20156 Milano, Italy

Abstract

Fatigue crack growth in composite, single lap bonded joints is analysed by back face distributed strain sensing, using optical backscatter reflectometry. Crack growth is inferred from the back-face strain profile measured with high spatial resolution along optical fibres bonded on the joints. The indications about the position of the crack front are compared with micro computed tomography scans conducted on specimens at suitable interruptions of the fatigue tests. By the proposed technique, crack initiation can be clearly detected, and measurements of crack growth are in good agreement with observations, with decreasing error with increasing crack length.

Keywords: fatigue crack propagation, distributed sensing, micro computed tomography, adhesive joints, composites

[*] Corresponding author: Tel. +39-02-23998222, Fax +39-02-23998202, E-mail: andrea.bernasconi@polimi.it

1. INTRODUCTION

Adhesive bonding is a joining technique particularly suitable for composite lightweight structures, because it adds less mass to the structure and induce less stress concentrations, compared to mechanical joints. However, to increase the level of acceptance by designers, proper non-destructive testing (NDT) and structural health monitoring (SHM) techniques are required, particularly for monitoring fatigue crack growth.

The present research focuses on a fatigue crack growth monitoring technique exploiting the Back-Face (BF) strain technique based on distributed strain sensing by Optical Backscatter Reflectometry (OBR) to monitor Fatigue Crack Growth (FCG) in adhesive joints between Carbon Fibre Reinforced Polymer (CFRP) adherends and compares its performance with micro computed tomography (μCT) observations.

The BF strain method consists of measuring strains on the back face of a joint, e.g. a single lap (SL) joint, using a single strain sensor or an array of sensors [1]-[2] and establishing a relationship between the signals recorded by the sensors and the position of the crack tip or front in the adhesive or in the composite substrates. Optical strain sensors are particularly suitable for monitoring FCG in adhesive joints [3] due to their small size, which makes it possible to embed them in the composite laminates, absence of sensitivity to electromagnetic fields and the absence of wiring. The BF strain technique was successfully applied using arrays of FBGs and standard electrical strain gauges to monitor fatigue crack propagation in a hybrid metal-CFRP adhesive joint [4]. In other works, FBGs were embedded in the joints, like in Canal et al. [5], where FBG arrays were embedded at three different positions through the thickness of the joints, or in Sans et al. [6] where FBG sensors were embedded inside the layer above the crack surface. Arrays of FBG sensors were used to monitor mode I propagation in unidirectional carbon fibre/epoxy Double Cantilever Beam (DCB) specimens by Stutz et al. [7] and Da Silva et al. [8] used FBG optical sensors to measure the strain distribution in adhesive joints.

Using FBGs, it is possible to inscribe and interrogate several gratings along the same fibre. An array of FBG sensors is a method to achieve an almost distributed strain sensing along the sensors' array. However, it requires careful identification of the position of the grating along the fibre and

accurate positioning, which requires bending the fibres to form loops in order to achieve small distances between the gratings, given the difficulty of inscribing gratings along a single fibre at small distance from one another. To avoid this, approaches which do not require arrays have been proposed. Yashiro et al. [9] developed a SHM method exploiting the full response spectrum of FBGs embedded in the bond line to monitor the crack growth. To achieve distributed sensing with only one grating, Chirped Fibre Bragg Grating (CFBG) sensors can be used. CFBGs were used by Sanderson et al. [10] to monitor delamination in composite DCB specimen, by Capell et al. [11] to monitor fatigue crack growth in hybrid composite/aluminium alloy single lap joint and by Palaniappan et al. [12] to monitor glass fibre reinforced single lap joints. To achieve distributed sensing with high spatial resolution with one single FBG, Optical Frequency Domain Reflectometry (OFDR) was applied to a long (e.g. 100 mm) FBG [13]. This technique allowed for a single lap joint between CFRP adherends under fatigue loading to be monitored [14].

Another way of achieving distributed sensing, in this case without any grating, is the Brillouin Optical Time Domain Reflectometry (BOTDR), which was successfully applied by Murayama et al. [15]. However, spatial resolution can hardly be lower than a few centimetres and it was improved to 1.6 mm by the Brillouin Optical Correlation Domain Analysis (BOCDA) [16].

The OBR technique [17] allows, again without the need to manufacture any artificial grating or sensor, to achieve distributed sensing with sub millimetric spatial resolution using a standard optical fibre connected to an OBR interrogator. Specifically, this technique applies swept wavelength interferometry to stimulate and acquire the Rayleigh backscattered light profile caused by the inherent defects distributed along the core of an optical fibre. The peculiar backscattered response of such defects, then, defines the reference fingerprint of a given optical fibre. The application of external thermal and/or mechanical stimuli (strains) to the optical fibre produces changes of the Rayleigh backscattered profile ([17], [18]) and such changes, after suitable calibration and comparison to the reference fingerprint, allow to back-estimate and quantify such external strains. Since the interrogator gathers a point-by-point response from the adopted fibre, strain measurements are distributed. The spatial resolution of this method is of a virtual kind, i.e., a virtual gage length is set by the user depending on the needs and can vary from fractions of millimetres to kilometres. Frövel et al. [19] and

Grave et al. [20] demonstrated the applicability of distributed sensing by OBR to composite structures, adhesive joints and bonded patch repairs [21].

The application of the BF strain technique using OBR distributed sensing, with one single optical fibre as sensing unit, was demonstrated in [22] for a woven CFRP SL joint. BF strains were measured by OBR at different levels of static loading. Experimental results showed that the adopted solution has a spatial accuracy which is high enough to detect the minimum peak of the BF strain profile and results were validated by Digital Image Correlation strain measurements. Then, to demonstrate the possibility of exploiting the BF strain monitoring technique by OBR distributed sensing to monitor FCG in bonded joints, similar tests were repeated under fatigue loading and results of the fatigue crack growth monitoring based on BF and OBR were compared with Visual Testing (VT) and Phased Array Ultrasonic Testing (PAUT) [23]. It was shown that the propagation of a crack in the joint causes a displacement of the negative peak of the BF strain, as shown schematically in Figure 1. A linear correlation between the position of this peak and that of the crack tip was found. A similar technique based on OBR distributed sensing was also applied to a composite step lap joint under fatigue loading and proved to be an effective SHM method [24].

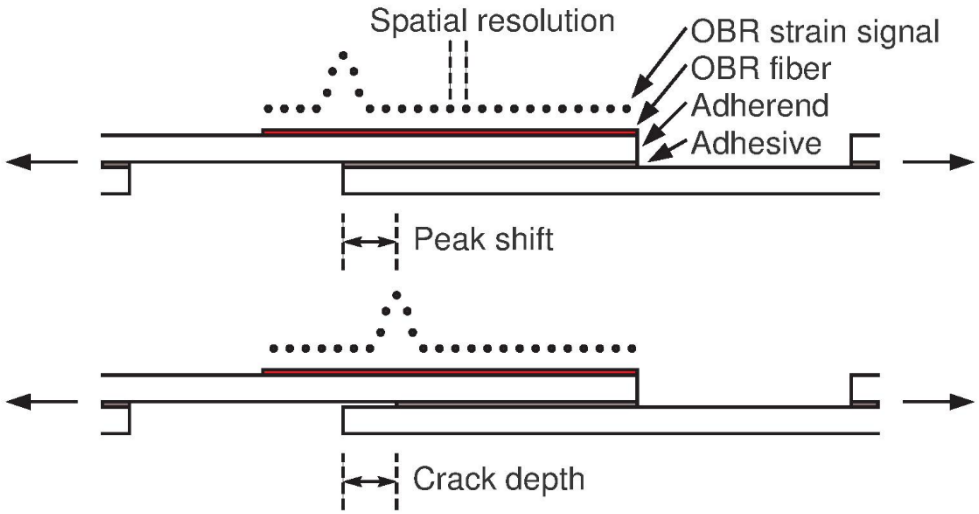

Figure 1 – Illustration of the displacement of the BF strain peak as the crack depth increases

The present paper extends and complement the results presented in [23], by adding observations of the 3D reconstruction of the fatigue cracks by μCT performed at suitable interruptions of the fatigue tests and, consequently, at different levels of damage development. In the literature, μCT proved to be an effective way of characterizing the damage of CFRP single-lap bolted joints [25]. It was used to observe the formation of pores in adhesive joints [26]-[29] and the evolution of damage in aluminium alloy spot weld joints with and without adhesive [30]. In the case of composite joints, observations of impact damage in composite single lap joints were reported in [31] and, in [32], it was demonstrated that μCT allowed for the observations of the evolution of fatigue damage in composite adhesively bonded scarf joints.

In this work, using specimens belonging to the same batch as those tested in [22] and [23], fatigue tests were monitored by the BF strain technique, based on OBR distributed measurements and by μCT reconstructions and VT carried out at different stages of the fatigue lives. This allowed to derive the actual position and shape of the crack front and to validate the fatigue crack growth measurements based on the OBR distributed sensing BF strain measurements. The possibility of performing OBR dynamic acquisitions without interrupting the tests is also discussed.

2. EXPERIMENTAL

2.1 Materials and specimens

Tests were conducted on three low modulus CFRP-CFRP single lap bonded joints, named #2, #3 and #4, having the shape and the dimensions reported in Figure 2. The adherends were woven CFRP laminates (twill weave) having a stacking sequence $[+45/0_2/+45]_S$ of 0.66 mm thick plies, for a total thickness of 5.3 mm. Laminates were fabricated by autoclave curing of prepregs. Table 1 reports the elastic constants [23] of the involved CFRP laminate. The indexes 1, 2 and 3 refer to the longitudinal, transverse and out-of-plane directions.

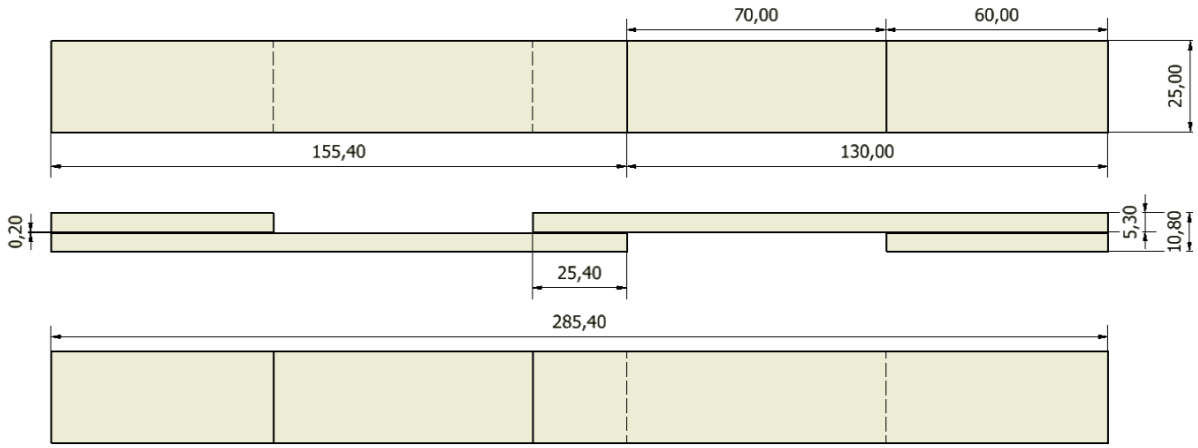

Figure 2 – Single lap CFRP-CFRP specimen shape and dimensions

Table. 1 – Elastic constants of the involved materials

	Young's moduli	**Shear moduli**	**Poisson ratios**
	[MPa]	**[MPa]**	**[]**
Adherend	$E_1 = 54500$	$G_{12} = 5000$	$\nu_{12} = 0.025$
	$E_2 = 54500$	$G_{13} = 2000$	$\nu_{13} = 0.25$
	$E_3 = 8000$	$G_{23} = 2000$	$\nu_{23} = 0.25$
Adhesive	$E = 2870$	$G = 1050$	$\nu = 0.37$

The described adherends were bonded by secondary bonding, with an overlap of 25.4 mm (Figure 2), using an epoxy structural adhesive Scotch Weld 9323 B/A resin, whose elastic constants [33] are reported in Table 1. Before bonding, the surfaces were prepared by cleaning using acetone, light abrasion with abrasive pads, and cleaning. The uniform thickness of the adhesive layer was guaranteed either by 0.2 mm diameter glass spheres (specimens #2 and #4) or by copper wires with a diameter of 0.2 mm (specimen #3). Two CFRP end tabs were also bonded to the specimens' ends to keep the load axis centred during fatigue tests.

2.2 Fatigue tests

All the here-mentioned fatigue tests were carried out (Figure 3a) in controlled load conditions, using a uni-axial MTS 810 servo-hydraulic testing machine of 100 kN capacity, at a frequency of 5 Hz and with a fatigue ratio R = min load / max load equal to 0.05.

In order to design effectively the test programme and to derive the fatigue load levels to be applied to the studied specimens, some preliminary fatigue tests were carried out to determine the first approximation S-N curves for both cases of adopted spacers: glass spheres (Figure 3b) and copper wires (Figure 3c). In Figure 3b and c, the load levels are normalized with respect to the ones eventually chosen for the strain profile monitoring tests using OBR.

The test load levels were, then, chosen to ensure an expected fatigue life of, at least, 500.000 cycles (Figure 3). Each test was periodically interrupted to get VT pictures of damage development and, particularly, at two specific time intervals, for each tested specimen, to carry out μCT scans along with VT acquisitions. Nevertheless, all tests were terminated just after the second interruption for μCT scanning without reaching the final failure of the tested specimens. Table 2 shows, for each tested specimen, the number of cycles of the applied interruptions for μCT scanning and the corresponding life percentage with respect to its expected (mean) fatigue life calculated according to the S-N diagrams reported in Figure 3. As can be seen and to the aim of considering different scenarios of damage development, the three tests were interrupted and μCT scanned at loads corresponding to a low number of expected fatigue cycles to failure (specimen #4), at an intermediate one (specimen #3) and at a high one (specimen #2).

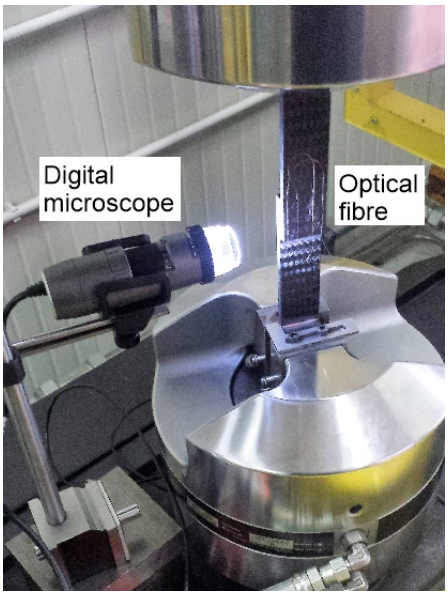

(a)

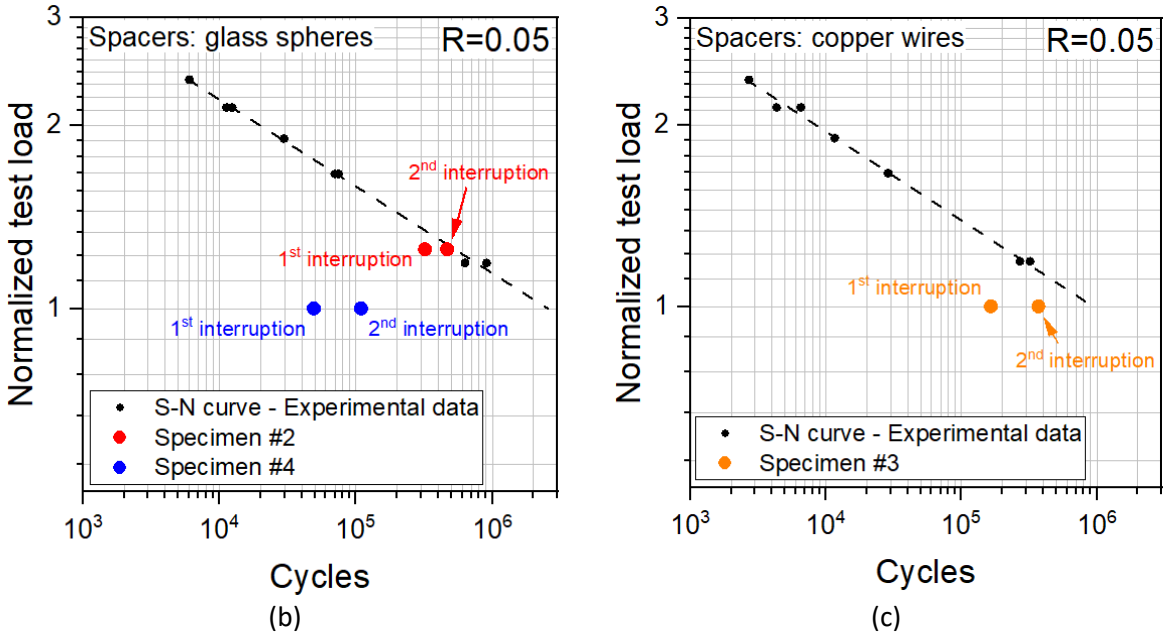

Figure 3 – Experimental setup (a) and S-N curves, showing the interrupted tests of the batch with glass spacers (b) and copper wires spacers (c)

Tab. 2 – Number of cycles at which fatigue tests were interrupted for μCT scans

Specimen	**1st interruption (Percentage of expected fatigue life)**	**2nd interruption (Percentage of expected fatigue life)**
	[cycles] ([%])	**[cycles] ([%])**
#2	321630 (61)	466359 (88)
#3	165000 (18)	405000 (40)
#4	49100 (2)	109000 (4)

2.3 Optical backscatter reflectometry

Each specimen was instrumented with a single 2.2 m long optical fibre ("Strain sensor 2m" by Luna Innovations Inc.) equipped with an LC/APC connector and a low reflection ending. The optical fibre was bonded, using a Z70 cyano-acrylate based rapid adhesive, on both external surfaces of the overlapped region of the given specimen. In particular, as can be seen in Figure 3a and Figure 4a, the fibre was properly shaped in order to provide four measuring segments, numbered 1, 2, 3 and 4 on one side ("front" side, which is the one the fibre approaches the specimen from) and 5, 6, 7 and 8 on the other one ("back" side, which is the one the fibre leaves the specimen from), of the specimens. In the

rest of the paper, these segments will be referred to using the number of the specimen and the number of the segment, separated by a point (e.g. segment 3.5 will indicate segment 5 of specimen #3).

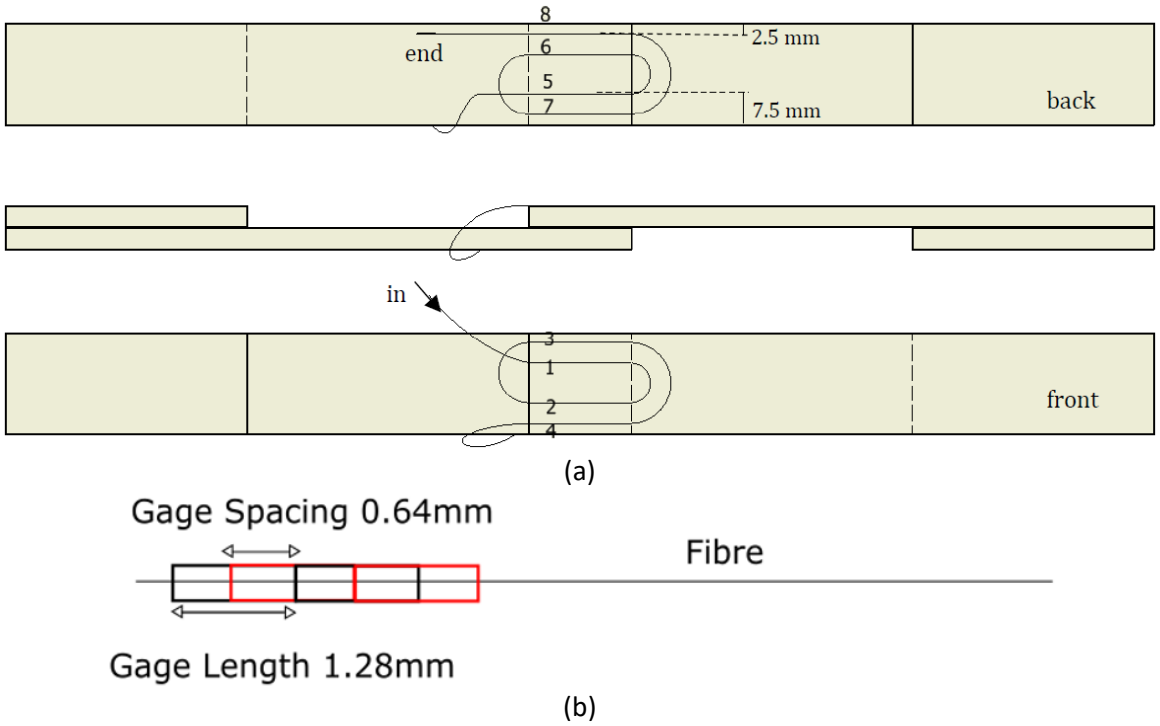

Figure 4 – Position of the optical fibre segments used for the BF strain measurements (a) and the adopted spatial resolution (b)

The fibre was, then, connected to an OBR interrogator ("ODiSI-B" by Luna Innovation Inc.), which was linked to a PC for data elaboration, storage and visualization. The interrogator allowed setting the spatial resolution of strain measurements: a virtual gauge length of 1.28 mm, with a gauge separation of 0.64 mm, was adopted (Figure 4b). BF strain values were recorded before starting any fatigue tests ("baseline" measurement) and at each test interruption aimed at carrying out VT inspections and μCT scanning. In particular, the baseline measurement and those at interruptions were acquired statically, applying a load equal to the maximum one of the applied fatigue cycle, and consisted in multiple acquisitions (about 1000) with the aim to define an averaged more stable reference profile likely affected by a lower level of noise. Nevertheless, additional dynamic, i.e. instantaneous and non-averaged, strain recordings were performed every 77s during the fatigue tests

without any interruption. These dynamic acquisitions have the purpose to evaluate the possibility of adopting OBR as an in-situ and real time strain sensing technique.

2.4 Visual testing

VT was carried out to evaluate the position and size of the outcropping tips of the fatigue cracks initiating at and propagating from the ends of the overlapped region. The set-up consisted of a high magnification Dino-Lite digital microscope supported by a gooseneck stand and a LED lamp used to light up the target surface (Figure 3a). This VT setup fully complies with the requirement of the ISO 25217 standard for mode I propagation in adhesives [35], which prescribes the use of "a travelling microscope or video camera, with suitable magnification, capable of measuring the crack length along the edge of the specimen to an accuracy of at least ± 0.5 mm."

2.5 Micro-computed tomography

Before starting any fatigue tests and at the test interruptions shown in Figure 3, specimens were inspected through x-rays μCT scanning performed by a North Star Imaging (NSI) X25 μCT scanner (Figure 5a). X25 is a four-axis, digital radiography and computed tomography system equipped with a micro-focus X-RayWor XTC tube having a voltage range between 10 kV and 160 kV (maximum power equal to 10 W). The detector is an x-rays flat panel characterised by an active area of 145.4×114.9 mm^2 and a pixel matrix of 1944×1536 pixels. The 3D reconstruction of the scanned volumes and their post-processing were carried out by NSI efX-ct v. 1.2 software package.

The region of interest (ROI) analysed by μCT scans consisted of the overlap region of the specimens. As an example, Figure 5b shows the 3D reconstruction of specimen #4 before starting its fatigue test, i.e. at 0 applied fatigue cycles. The parameters adopted for scanning all the specimens consisted in a voltage of 76 kV, an amperage of 40 μA, a focal spot size of 3 μm and a magnification of 4x (focus-to-object distance equal to 187 mm and focus-to-detector distance equal to 740 mm). Adopting these parameters, the voxel size resulted to be equal to 18 μm. The number of projections was equal to 1200 on a full 360° rotation of the specimens and no filters were applied. To increase the

image contrast of damage with respect to the base material and the adhesive, a contrast medium (1,4 Diiodobutane ≥ 99% containing copper particles) was applied.

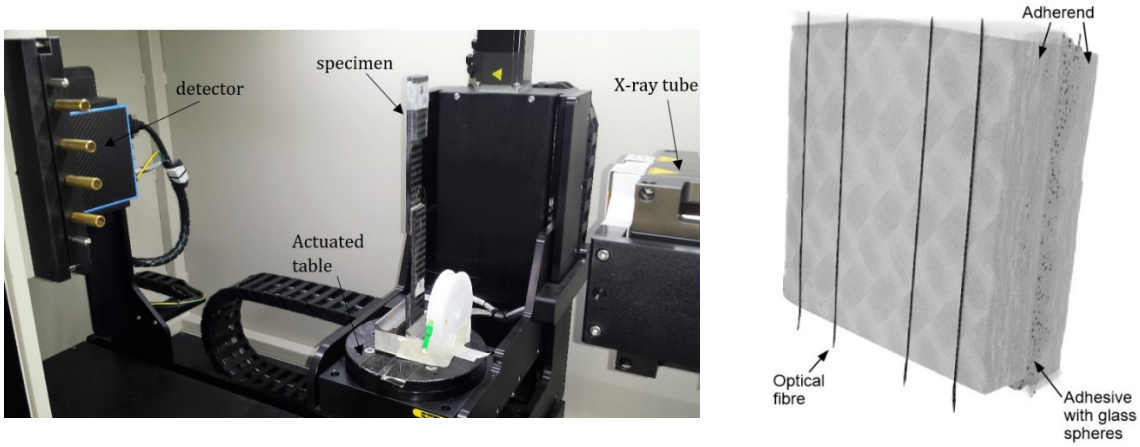

Figure 5 – μCT scanner (a) and 3D reconstruction of the ROI of specimen #4 (b)

3. RESULTS

3.1 Optical backscatter reflectometry

3.1.1 Static acquisitions

Figure 6a shows, for the exemplificative case of specimen #3, the baseline back-face strain profile compared to the one acquired at the first test interruption, after 165.000 fatigue cycles (18% of the expected fatigue life), and at the second interruption, after 405.00 fatigue cycles (40% of the expected fatigue life). Note that the baseline acquisition was recorded at the mean value of the fatigue load cycles, to avoid damaging the specimens before testing, while the acquisitions at the interruptions were performed at the maximum load. This justifies the difference in strain peaks between the baseline and the following acquisitions. Moreover, it is worth mentioning that the depicted strain profiles were rectified (taken as absolute values) for the sake of clarity.

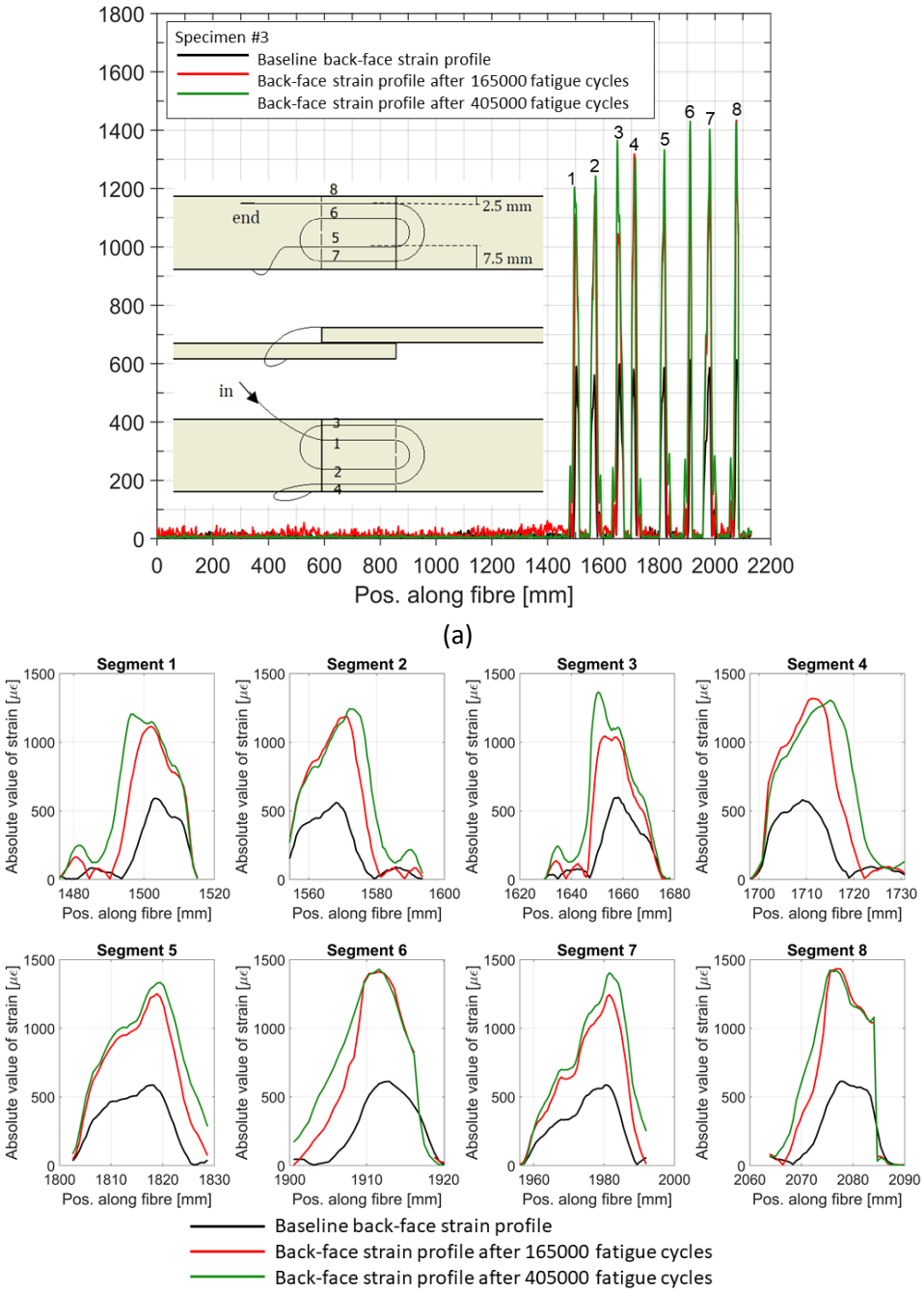

Figure 6 – BF strain profiles recorded by OBR at the beginning of the fatigue tests (baseline) and at test interruptions for μCT scans (exemplificative case of specimen #3): a) entire optical fibre and b) zoom on the eight considered segments.

As already observed elsewhere [22], the strain peaks of the baseline BF strain profile correspond to the edges of the overlapped region, indicating that the joint is fully intact at the beginning of the test. Then, with the application of fatigue loading, two different phenomena were observed:

1. the magnitude of strain peaks varied significantly (Figure 6a). Specifically, the average of the eight back-face strain peaks was 1178 με for the baseline profile, 1301 με after 165.000 fatigue cycles and 1339 με after 405.000 fatigue cycles. This can be likely explained as an effect of the loss of stiffness of the joint due to the development of fatigue damage;
2. strain peaks moved along the fibre with respect to their initial position in the baseline condition (Figure 6b). According to the assumed BF strain approach based on distributed sensing, the amount of peak shift should be directly correlated to crack propagation into the bonded joint (which can take place in the bond-line, in the composite, or at the interface between adhesive and substrates). This point will be discussed in the following sections of the manuscript. Note also that the load bearing area becomes wider as the disbond grows. This was also observed in [23]: with a smaller bonded area, the lap joint becomes more compliant, with the arms of the joint undergoing higher rotation. Therefore, strain values are higher and the region of the adherends undergoing higher strain becomes larger.

Figure 6b also highlights different strain profiles for the different segments. The strain seems not to vary linearly, but rather presents oscillations. This was already observed in [22], and correctly attributed to the weave orientation of the textile adherends. The influence of such a non-linear strain profile on the strain measurements will be discussed in Section 4.2.

Specimens #2 and #4 showed similar results and Table 3, Table 4 and Table 5 summarize the shifts of the BF strain peaks for all the eight measuring fibre segments of specimen #2, #3 and #4, respectively. In particular, such shifts were evaluated by simply calculating the difference between the coordinate of the peak values of the baseline condition and those after the application of fatigue loading.

Generally, it can be observed that the higher the number of applied fatigue cycles, the larger the measured peak shift. This evidence supports the existence of the expected correlation between crack propagation and peak shift. On the other hand, it is also worth noting that the peak shifts related to the four measuring segments located on the same side of a given specimen are generally not consistent,

suggesting the onset of a complex damage phenomenon occurring under each single segment of the optical fibre. This point will be discussed in Section 4.

Tab. 3 – Position of the strain peak measured by OBR, position of the crack front detected by μCT and corresponding error for specimen #2

At 321.630 fatigue cycles (1st interruption)								
	Front				Back			
Fibre segment	1	2	3	4	5	6	7	8
Peak shift (OBR) [mm]	5.2	4.6	6.5	5.2	6.5	7.2	10.4	7.8
Damage size (μCT) [mm]	4.7	5.7	6.7	5.5	7.2	7.1	9.4	7.1
Absolute error (OBR-μCT) [mm]	0.5	-1.1	-0.2	-0.3	-0.7	0.1	1.0	0.7
At 466.359 fatigue cycles (2nd interruption)								
	Front				Back			
Fibre segment	1	2	3	4	5	6	7	8
Peak shift (OBR) [mm]	11.8	10.4	7.8	10.5	6.5	7.2	11.1	8.5
Damage size (μCT) [mm]	9.9	9.4	8.1	10.1	7.9	9.1	9.8	8.8
Absolute error (OBR-μCT) [mm]	1.9	1.0	-0.3	0.4	-1.4	-1.9	1.3	-0.3

Tab. 4- Position of the strain peak measured by OBR, position of the crack front detected by μCT and corresponding error for specimen #3

At 165.000 fatigue cycles (1st interruption)								
	Front				Back			
Fibre segment	1	2	3	4	5	6	7	8
Peak shift (OBR) [mm]	1.3	3.3	5.2	2.0	0.6	0.6	1.3	0.6
Damage size (μCT) [mm]	2.3	2.4	4.3	1.2	0.0	0.0	0.0	0.0
Absolute error (OBR-μCT) [mm]	-1.0	0.9	0.9	0.8	0.6	0.6	1.3	0.6
At 405.000 fatigue cycles (2nd interruption)								
	Front				Back			
Fibre segment	1	2	3	4	5	6	7	8
Peak shift (OBR) [mm]	6.5	3.9	7.8	5.8	1.3	0.6	1.3	2.0
Damage size (μCT) [mm]	5.5	3.4	6.0	3.8	0.0	0.0	0.0	2.5
Absolute error (OBR-μCT) [mm]	1.0	0.5	1.8	2.0	1.3	0.6	1.3	-0.5

Tab. 5 - Position of the strain peak measured by OBR, position of the crack front detected by μCT and corresponding error for specimen #4

At 49.100 fatigue cycles (1st interruption)								
	Front				Back			
Fibre segment	1	2	3	4	5	6	7	8
Peak shift (OBR) [mm]	0.0	0.0	0.0	1.3	0.65	0.0	0.0	1.3
Damage size (μCT) [mm]	1.2	1.1	0.8	0.1	0.0	0.0	0.0	0.0
Absolute error (OBR-μCT) [mm]	-1.2	-1.1	-0.8	1.2	0.65	0.0	0.0	1.3
At 109.000 fatigue cycles (2nd interruption)								
	Front				Back			
Fibre segment	1	2	3	4	5	6	7	8
Peak shift (OBR) [mm]	1.3	1.3	1.96	1.96	1.96	1.96	1.96	2.6
Damage size (μCT) [mm]	3.6	2.9	3.1	1.4	1.5	3.4	1.0	3.6
Absolute error (OBR-μCT) [mm]	-2.3	-1.6	-1.14	0.56	0.46	-1.44	0.96	-1.0

3.1.2 Dynamic acquisitions

The dynamic acquisitions were found to be more delicate and susceptible to noise and environmental influences: some of them were not able to capture any meaningful strain values in certain regions of the fibre. Indeed, LUNA user's guide [36] explains such dropouts are expected and typically due to external disturbances. When dropouts occurred within one of the segments, that entire segment acquisition was discarded.

Figure 7 shows the strain profile for all eight segments obtained with both static acquisitions at the maximum fatigue force (in red) and at half of its value (in blue) and the dynamic acquisitions, for specimen #2. The static acquisitions were performed at the last interruption, after 405.000 cycles. The reported dynamic acquisitions are the exemplificative case of those obtained between 370.000 cycles and 405.000 cycles. The different number of dynamic acquisitions for the different segments are due to the aforementioned dropouts filter.

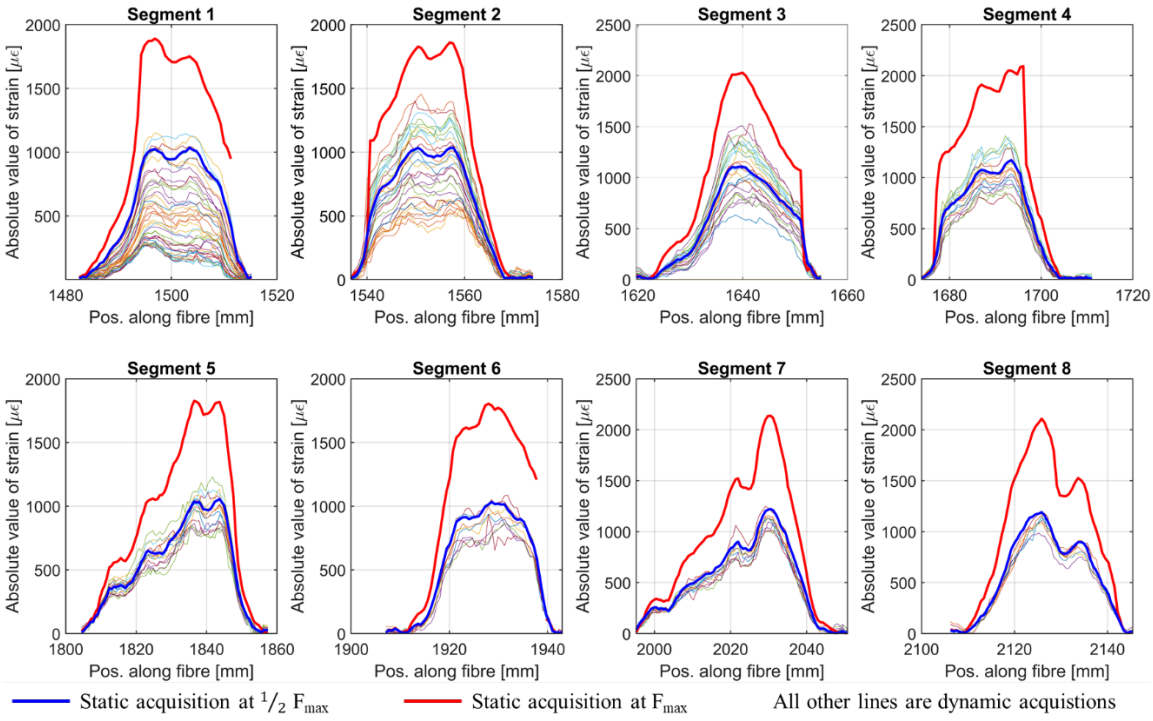

Figure 7 – Strain profile comparisons between static and dynamic acquisitions for specimen #2. The static acquisitions were performed at the second interruption, at 405.000 cycles; the reported dynamic acquisitions are obtained between 370.000 and 405.000 cycles.

Overall, the strain profiles measured by the dynamic acquisitions show the same qualitative trend with respect to the static ones. Moreover, it was verified that the dynamic acquisitions performed during fatigue loading yielded results that did not differ significantly from static acquisitions (comparison was performed extracting from the available strain profiles acquired dynamically and shown in Figure 7 those recorded when the load was as close as possible to the one applied during static acquisitions). Only some minor differences were observed because dynamic acquisitions are more susceptible to noise. Therefore, it can be concluded that OBR can acquire the strain profile in the specimen fast enough for the acquisitions not to be affected by the variation of strains over time.

The peak shifts of the dynamic acquisitions for specimens #2, #3 and #4 are reported in Figure 8, Figure 9 and Figure 10, respectively. The vertical discretization of the data immediately reveals the influence of the spatial resolution of the optical fibre.

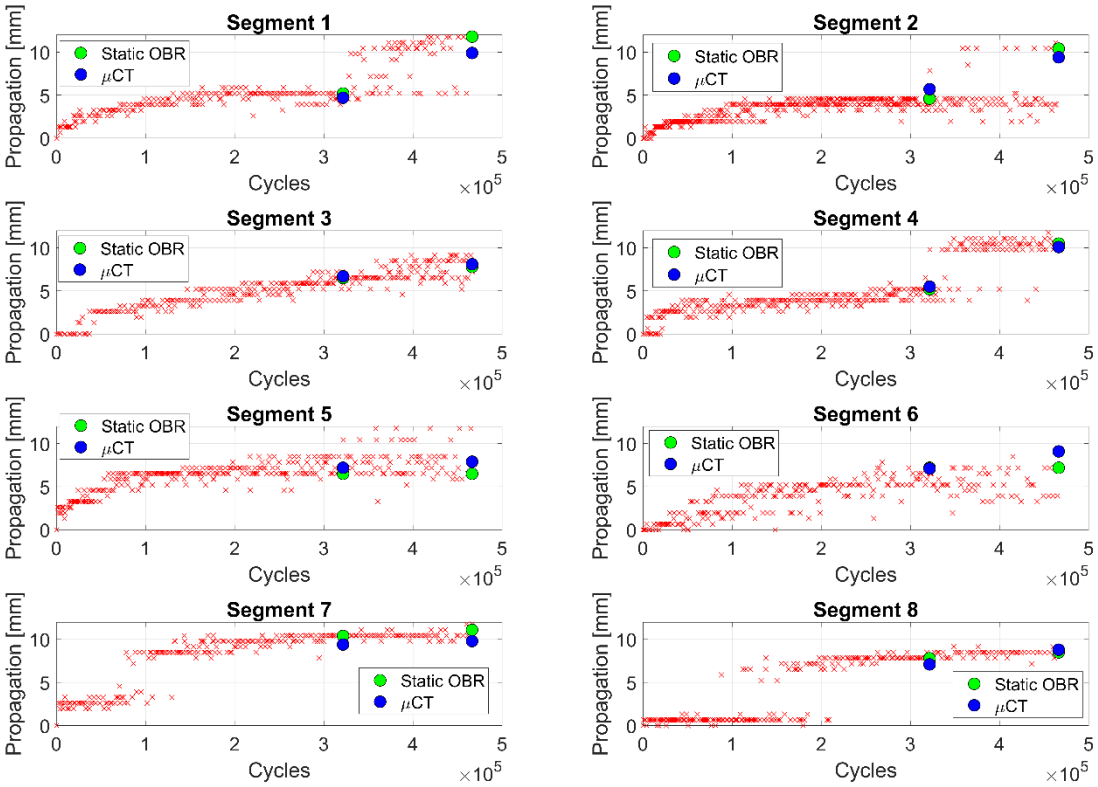

Figure 8 – Peak shifts (red crosses) during the lifetime of specimen #2, compared with the static acquisitions and μCT observations.

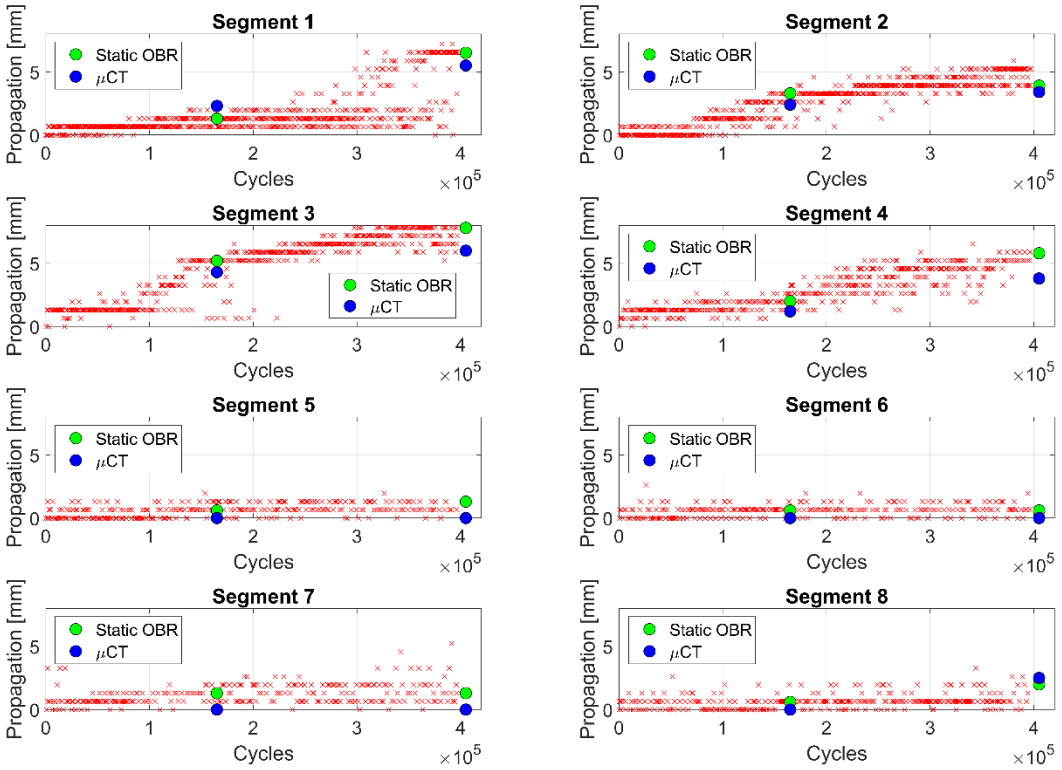

Figure 9 – Peak shifts (red crosses) during the lifetime of specimen #3, compared with the static acquisitions and μCT observations.

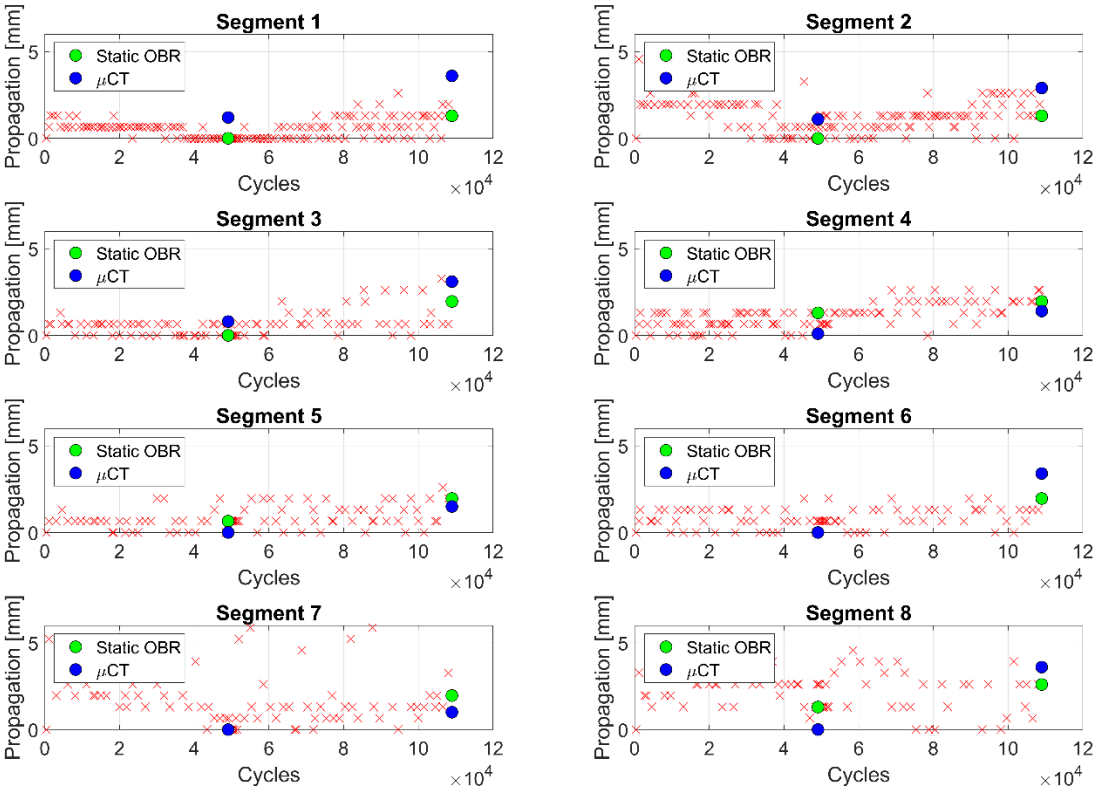

Figure 10 – Peak shifts (red crosses) during the lifetime of specimen #4, compared with the static acquisitions and μCT observations.

Overall, the trends identified by the dynamic acquisitions are in good agreement with the static OBR acquisitions and the μCT observations, although a significant standard deviation is present. Segments 2.1, 2.2, 2.4, 2.7, 2.8 and 3.1 all show a step-like shifting behaviour of the strain peaks. This feature can be explained by comparing Figure 7 and Figure 8. The static strain profiles for segment 2.1, for example, present two peaks caused by the morphology of the textile adherends (as explained before). Figure 7 shows that only at the maximum applied force one of the two peaks is clearly higher than the other one. In the strain profile relative to half of the maximum force, the difference between the peaks is very small. The frequency of the dynamic acquisitions and the load frequency are relatively prime, and therefore dynamic acquisitions are not performed always at the same load level of the fatigue cycle. Therefore, the relative strain profiles are more scattered around the mid-force strain profile, and thus have a more similar shape to those profiles than that at maximum force. The difference between the peaks in the dynamic acquisitions profiles is thus not large enough to consistently identify one of the peaks as bigger in all cases, and the peak value is thus taken alternatively as one of the two. Segments 2.2 and 3.1 seem to be more subjected to this problem, since

the dynamic acquisitions revealed a different maximum peak than that considered by the static acquisition at maximum load. For the other segments, the peak evaluated by dynamic acquisitions is the same as that of the static ones.

3.2 Visual testing

Figure 11a shows, as an example, the pictures taken, at different amounts of applied fatigue cycles, at one of the four corner edges of the overlap region of specimen #3, while the top view of the same specimen, at the second interruption of its fatigue test, is shown in Figure 11b. As can be seen, the development of fatigue damage is clearly evident. When a crack initiates in the adhesive and becomes visible on the side of the specimen, it appears as a white line. Whitening is likely to be related to the local plasticization of the polymer at the crack tip. Similar observations were reported in [34] for the same adhesive type under fatigue loading. A crack in the adhesive of specimen #3 appeared at 165,000 cycles, when the tests was interrupted for the first time. Then, it propagated with an inclination of 45° with respect to the specimen's main axis until it reached the interface between the adhesive and the substrate. From 220,000 cycles onward, the trace of the crack emerging on the side of the specimens propagated along this interface.

Figure 11c shows the example of one of the corner edges of specimen #2 at the first interruption of its fatigue test. Like in specimen #3, also in this case a crack appeared at one overlap end, in the small adhesive fillet, and then propagated, partly in the adhesive, partly at the interface between the adhesive and one adherend. This kind of VT static monitoring was carried out for all four-corner edges of all the three tested specimens, at the test interruptions described in Section 2.2, to record initiation and propagation of damage, at least in terms of the surface cracks cropping at the sides of the specimens. The acquired pictures were digitally elaborated, after a suitable calibration of the pixel-length relationship, to size the evolution of the emerging damage and to collect data to be compared with the observation by the other methods.

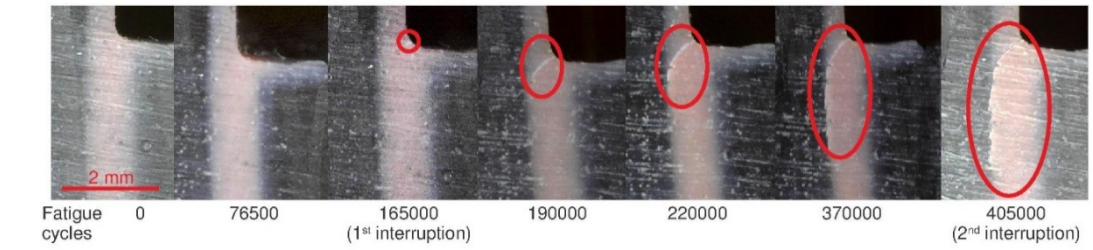

(a)

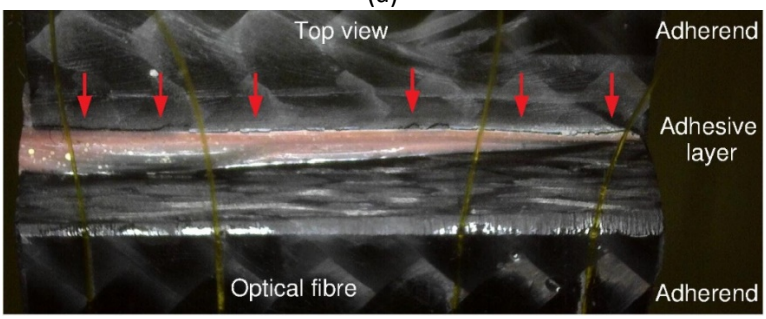

(b)

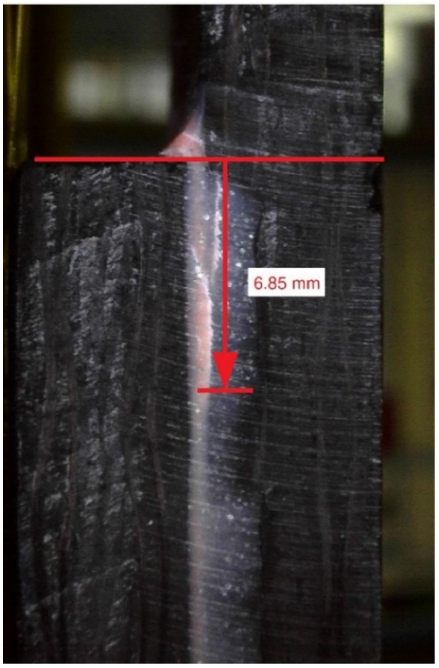

(c)

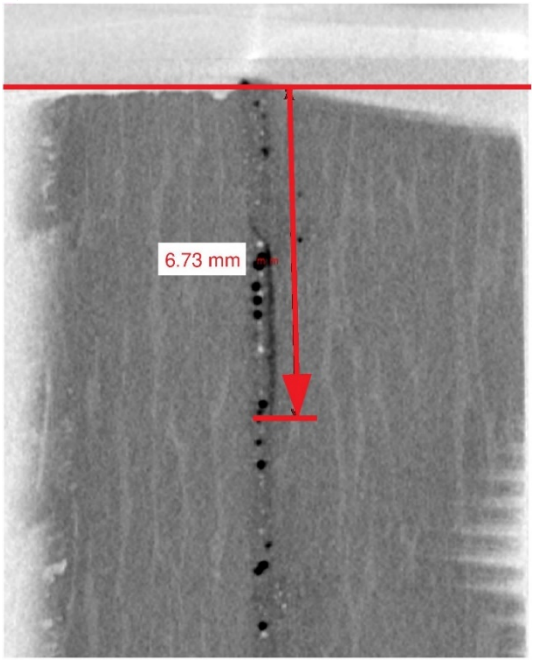

(d)

Figure 11 – VT observations of the fatigue cracks emerging at the side surfaces of the joints (a, specimen #3), top view (b, specimen #3), measurement of the crack length (c, specimen #2 – 1st interruption) and measurement of the same crack length by μCT (d, specimen #2 – 1st interruption)

3.3 Micro-computed tomography

The analysis of fatigue damage by μCT was performed observing the 3D reconstructed volumes of the tested specimens along suitable cutting planes (slices). Figure 12 showcases some μCT observations of specimens #2. In particular, Figure 12a shows specimen #2 at the second interruption of its fatigue test. This μCT slice allows for highly contrasted features to be visualized. Similar

features could be also observed at the bottom edge, but they could not be visualized in the same figure because lying in a neighbouring, slightly shifted and parallel, slice, as shown in Figure 12b. It is worth remarking that these features were not observed before starting the fatigue test, so it is reasonable to assume they are related to the onset and development of fatigue damage. It is worth noting that the features associated to fatigue damage form a rather complex geometrical pattern and clearly follows preferential paths related to the local morphology and structure of the woven laminate.

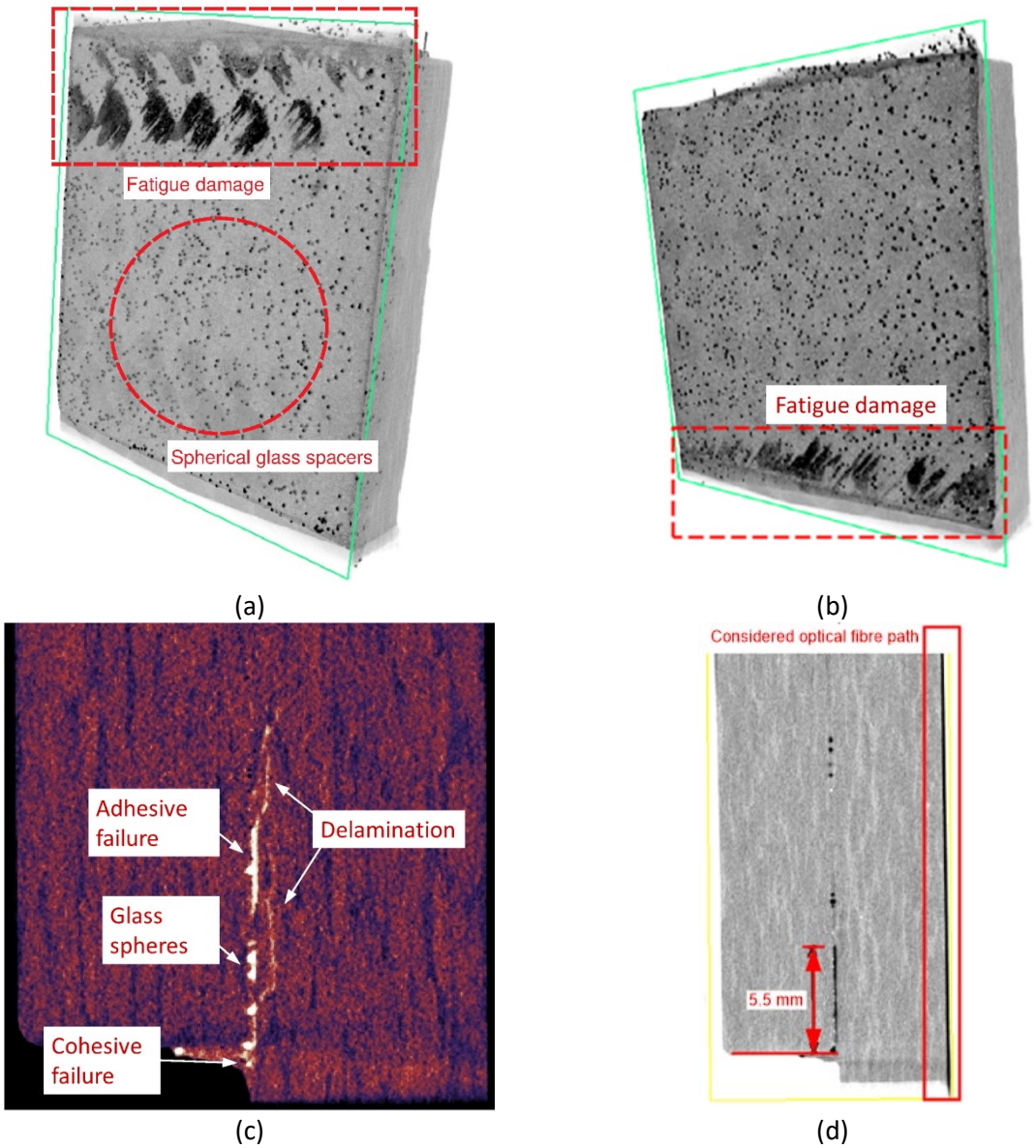

Figure 12 – µCT reconstruction of the fatigue crack in specimen #2: top edge at the 2nd interruption of its fatigue test (a), bottom edge at the 1st interruption of its fatigue test (b), transverse slice at the 1st interruption of its fatigue test (c), crack length measurements below optical fibre segment #4 at the 1st interruption of its fatigue test (d)

To get more insight, Figure 12c showcases, by false colours in order to further enhance contrast, the detail of a transversal slice of the case reported in Figure 12b. The assumed correlation between the contrasted features and fatigue damage is supported by the clearly apparent crack-like morphology of the transversal section of the contrasted features themselves. It is also worth observing that the shown fatigue damage is not characterized or dominated by a single failure mode, but both the adhesive and the adherends are simultaneously involved. In particular, the crack initiates in the adhesive fillet with a cohesive failure mechanism and then propagates both inside the adherends, as a delamination, and along the adhesive/adherend interface, as an adhesive failure.

Eventually, by means of transversal slices of the 3D reconstructed μCT volume and a suitable calibration of the pixel-length relationship, damage size and failure modes could be highlighted and measured beneath each optical sensing segment. The exemplificative case of specimen #2, at the first interruption of its fatigue test and in correspondence of segment #4, is shown in Figure 12d.

This procedure was applied systematically to all the tested specimens at their interruptions and the results are summarized in Table 3, Table 4 and Table 5.

4. DISCUSSION

4.1 Accuracy of the considered methods

The data collected during the experiments were analysed to assess the relationship between the shifts of OBR strain peaks and the damage size estimated by μCT scans. To this aim, the accuracy of the results obtained by μCT was first assessed, by comparing the size of the crack-like damage, measured by VT on the lateral surfaces of the specimens, to the one present on the lateral side of the corresponding 3D reconstructed μCT volumes. An example of this comparison is given in Figure 11c and Figure 11d for the case of specimen #2 at the first interruption of its fatigue test. As can be seen, μCT provides a rather accurate reconstruction of the actual morphology and size of the fatigue damage, at least of the one emerging on the lateral side of the specimen. This was generally observed for all corner edges of all the overlapped regions of the specimens at all interruptions. Consequently,

it seems that the effective implementation of the μCT scanning procedure, for the case at hand, can be confirmed and it is here assumed that μCT is sufficiently accurate to be a reference comparison for the results obtained by OBR.

Table 3, Table 4 and Table 5 show the complete comparison between the peak shifts measured by OBR and the corresponding damage sizes estimated by μCT for specimens #2, #3 and #4 at their interruptions, respectively. Data of some relevant cases are also plotted in Figure 13.

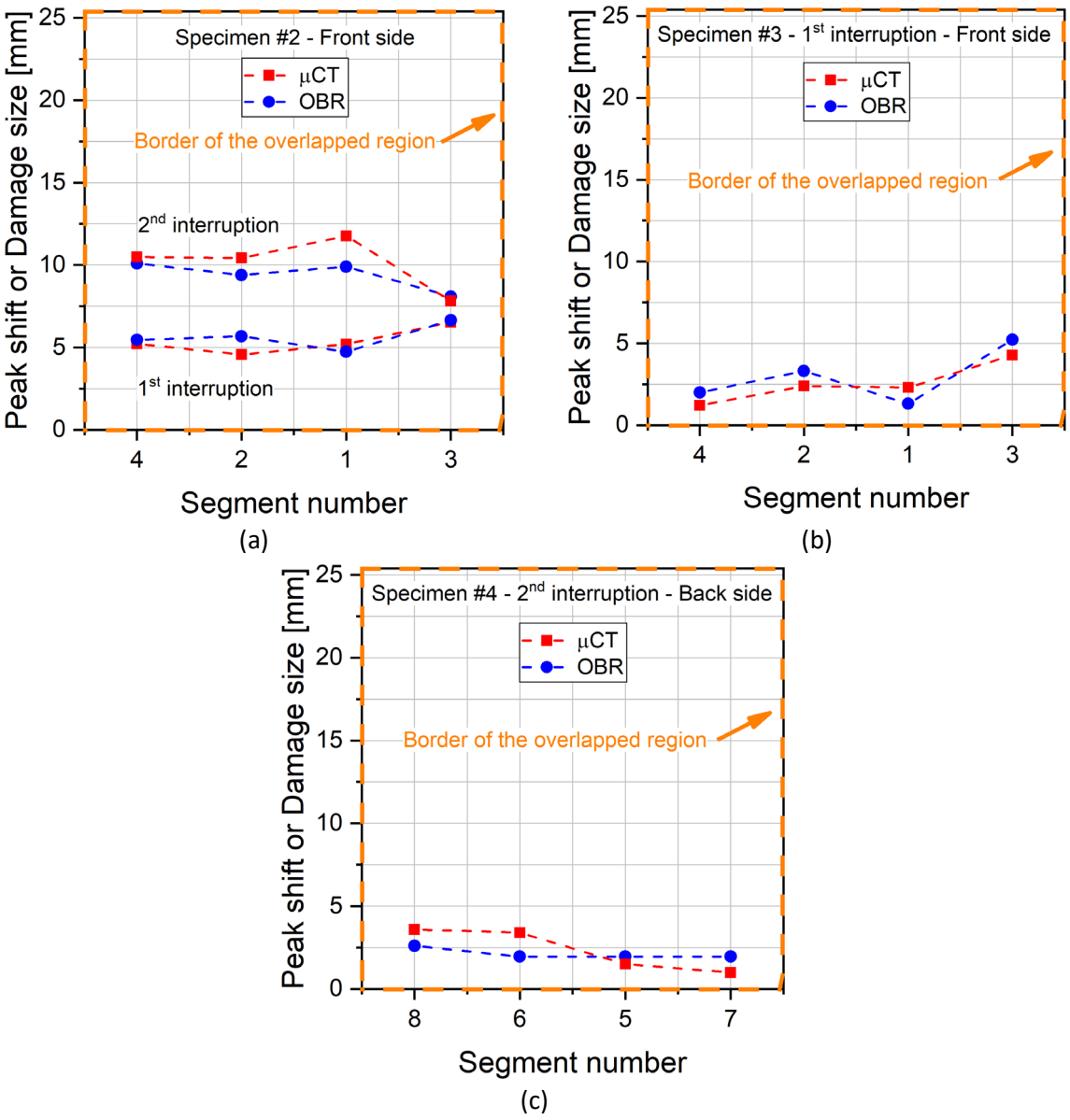

Figure 13 – Some examples of BF strain peak shifts and comparison with the corresponding μCT measurements for specimen #2 (a), #3 (b) and #4 (c)

From a qualitative point of view, a first remark is that both the measurement of peak shifts by OBR and the estimation of damage size by μCT systematically increase, as expected, with the accumulation of fatigue cycles. Based on these observations, an advancing crack front can be reconstructed, see Figure 13a for an exemplificative case. Moreover, both methods highlight (Figure 13), in a consistent way, the irregular and complex damage morphology, driven by the local microstructure of the woven laminates, already pointed out in Section 3.3.

Quantitatively, the agreement between the two methods is reasonably good. Figure 14a shows the whole set of experimental data reported in Tables 3, 4 and 5 plotted in terms of peak shifts, measured by OBR, against damage sizes, estimated by μCT. The linear regression and its 95% confidence band, both derived by the maximum likelihood method, along with the ideal trend (45° line) are shown, as well. As can be seen, the hypothesis about the existence of a statistically significant linear correlation between OBR data and μCT ones is confirmed by the determination coefficient R^2, which assumes a value equal to 0.9081. Moreover, the linear regression, characterized by a slope close to 1 and an intercept close to 0, highlights an excellent agreement with the ideal trend. In particular, such an agreement is mainly supported by the observation that the ideal trend is included within the confidence band of the regression line for the whole range of the experimental data: this involves a statistical identity between the two lines.

Considering the scatter of the experimental data around the regression line, Figure 14b shows the distribution of the "absolute error", defined as the difference between each peak shift measured by OBR and the corresponding damage size estimated by μCT. As can be seen, it seems to be rather uniform over the whole range of estimated damage sizes and, consequently, to be uncorrelated to them. In order to rigorously check such a statement, a regression analysis was carried out: the application of many different regression curves (polynomials of order from 1 to 6, exponential, power law and logarithmic) provided values of the determination coefficient R^2 ranging from 0.005 to 0.3, confirming the supposed lack of correlation between absolute error and damage size.

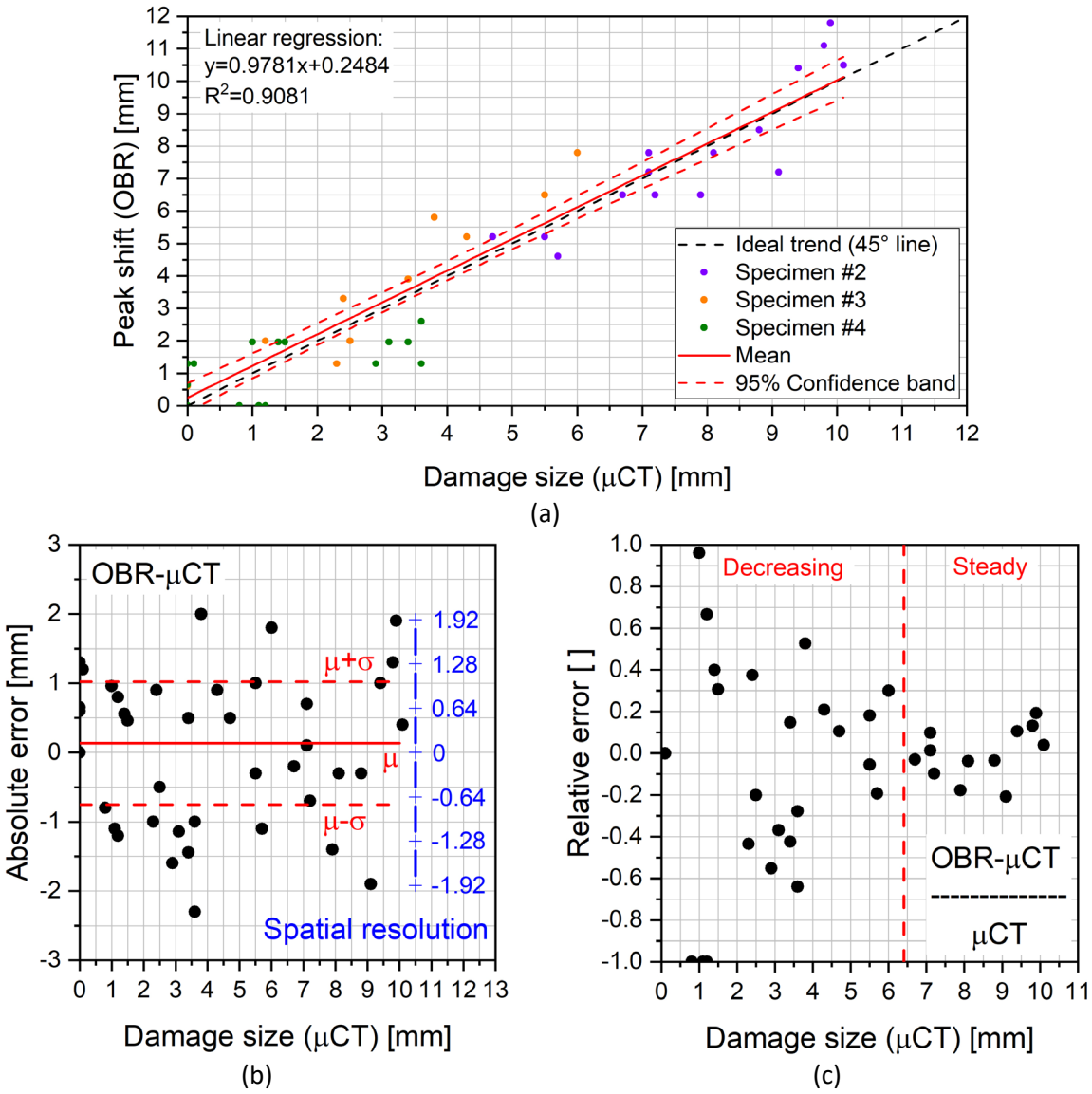

Figure 14 – Relationship between BF strain peak shift and damage size reconstructed by μCT (a), absolute error and damage size (b), relative error and damage size (c) for all specimens

From a quantitative point of view, the mean value μ of the absolute error equals 0.17 mm with a standard deviation σ of 1.07 mm and with a maximum absolute value of about 2 mm in a few cases, but, on the other hand, with a significantly lower one in many others. In particular, as can be observed, the mean value tends to zero, as expected, while the standard deviation results to be comparable to the spatial resolution of the applied OBR measurements, i.e. 0.64 mm (see Section 2.3 and Figure 4). From this point of view, most of the points fall, in terms of absolute value, within twice the value of such a spatial resolution (Figure 14b), which actually corresponds to the best (lower)

value provided, today, by OBR interrogators: a better resolution, even if not yet technically available, might prospectively improve the accuracy of results. Indeed, for the case at hand where the damage sizes estimated by μCT ranges from below the value of the spatial resolution of OBR to significantly higher ones, the relative error, defined as the absolute error normalized by the damage size estimated by μCT, clearly decreases with the increment of the estimated damage size (Fig 10c) up to about 6 – 6.5 mm, i.e. about ten times the spatial resolution of OBR, and then becomes steady within a maximum error band of ±20%.

Some other comments are worth being reported. The above-mentioned maximum value of the absolute error, i.e. about 2 mm, results to be comparable to the mean one of volumetric NDT manual inspections applied to similar specimens by means of phased array ultrasonic testing (PAUT) [23], prospectively suggesting a better accuracy of OBR with respect to PAUT. Moreover, the observed scatter of the absolute error is not just originated by the spatial resolution of OBR. Another possible source of scatter is that, while μCT estimates are based on a direct evaluation of the position of the crack front in the sections (slices) of the reconstructed 3D volume corresponding to the location of the optical segments, OBR measurements might be someway influenced by the collaboration of the whole volume of material beneath and around the optical fibre and located between the optical fibre itself and the crack plane. This rationale, acting along with the irregular and complex morphology of the crack front, implies the introduction of a source of uncertainty, on the accuracy of OBR strain measurements, able to contribute to the observed scatter of experimental data.

4.2 Peak shifts behaviour

Both the static and dynamic OBR acquisitions are likely affected by the underlying adherend morphology. This assumption is supported by previous results. Non uniform strains were measured by Digital Image Correlation on the same material of the adherends of this work [37] using thinner specimens with all plies oriented at 0°. Moreover, oscillations of the strain values were measured by OBR under static loading on one specimen of this batch [22]. An oscillation wavelength of 10 mm equal to the size of the repeating unit structure of the woven material was reported. This wavelength is close to the distance between neighbouring peaks shown in Figure 6 and 7. Figure 6b, relative to

specimen #3, highlights different peak shifts behaviours: for most of the segments, an individual strain peak moves due to the presence of a propagating crack front. For segments 3.1 and 3.3, however, a new peak is created between the two interruptions. This is likely due to the interaction between the strain peak due to the crack front and an additional strain peak due to the weave orientation.

The adherend morphology might have a minor impact for the static OBR acquisitions, since they are performed at the maximum load of the fatigue cycle: the strain peak due to the crack likely overcomes the presence of the peaks due to the weave orientation. However, dynamic acquisitions are likely to be more affected by the morphology and structure of the material, as they are more commonly performed at lower force levels. The comparisons of Figure 7 and Figure 8 and also of Figure 6 and Figure 9 show another possible peak shift behaviour, indeed. The adherend weave orientation tends to create two strain peaks, and the presence of the crack only makes one of the two bigger than the other. When the crack propagates from one peak location to the other, the highest of the two peaks changes accordingly. This results in a measured stepwise propagation even in the case of a stable constant propagation rate.

Finally, note that, while the entire strain profiles were briefly discussed in this section, only their peaks were used to evaluate the crack propagation in the adhesive. That is because the present work mainly evaluates the applicability of the peak strain shifts method as a crack propagation monitoring technique. The method was already presented in [22, 23] and was thus extensively analysed for static loads. It would also be possible to use the entire strain profile to evaluate the crack propagation in the adhesive. However, this would require a deeper understanding of the relation between damage and strain profile measured by the OBR, and thus a more extensive analysis that would be beyond the scope of this work. Nevertheless, this approach represents an interesting further development of the present technique.

5. CONCLUDING REMARKS

The back-face strain technique was applied to monitor the fatigue crack growth in single lap composite bonded joints, using distributed strain sensing techniques based on fibre optics and Optical

Backscatter Reflectometry. Micro computed tomography and visual testing were used to check the results obtained by the distributed sensing technique at certain stages of the fatigue life. Potentialities and limitations of the use of back-face strain as monitoring technique for cracks developing under fatigue loads are thus presented.

The results based on strain profile measurements at constant load were in good agreement, suggesting that the back-face strain technique can be used for crack monitoring under fatigue loads. It was however observed that the available spatial resolution of the used OBR system limits the possibility of accurately defining the actual crack size for damages smaller than 2 mm. On the other hand, for sufficiently large damages (6-6.5 mm), this method allows to detect, size and monitor the actual dimension of the cracks with a good accuracy.

Nevertheless, the maximum error of static measurements is comparable to, if not better than, the mean error of phased array ultrasonic testing, thus ensuring a comparable uncertainty in early damage detection by a structural health monitoring method based on OBR distributed sensing.

Dynamic acquisition performed during the fatigue load were also evaluated. The measured peak shift was in good agreement with the acquisitions performed at constant load, although a large scatter prevents their use as a stand-alone reliable strain sensing technique. Such data dispersion was mainly attributed to the adherend morphology and to the measurements performed at lower load levels.

ACKNOWLEDGEMENTS

The authors would like to thank Dr. A. Gianneo and Mr. A. Grossi for the active help given to the research. OBR measurements were carried out in the frame of the LAFOS Lab at Politecnico di Milano. μCT measurements were carried out in the frame of the AMALA Lab at Politecnico di Milano.

REFERENCES

[1] Zhehua Zhang, J. K. Shang & F. V. Lawrence Jr. A Backface Strain Technique for Detecting Fatigue Crack Initiation in Adhesive Joints, The Journal of Adhesion, 49 (1-2), 1995: 23-36

[2] A. D. Crocombe, C. Y. Ong, C. M. Chan, M. M. Abdel Wahab & I. A. Ashcroft Investigating Fatigue Damage Evolution in Adhesively Bonded Structures Using Backface Strain Measurement, The Journal of Adhesion, 78(9), 2002: 745-776

[3] Bernasconi, A., Carboni, M., Comolli, L., Monitoring of fatigue crack growth in composite adhesively bonded joints using Fiber Bragg Gratings. Procedia Eng. 10, 2011: 207–212

[4] Bernasconi A, Kharshiduzzaman M, Anodio LF, et al. Development of a monitoring system for crack growth in bonded single-lap joints based on the strain field and visualization by augmented reality. J Adhesion; 90(5–6) 2014: 496–510

[5] Canal, L. P., Sarfaraz, R., Violakis, G., Botsis, J., Michaud, V., Limberger, H. G. Monitoring strain gradients in adhesive composite joints by embedded fiber Bragg grating sensors. Compos. Struct., 112, 2014: 241-247

[6] Sans, D., Stutz, S., Renart, J., Mayugo, J. A., Botsis, Crack tip identification with long FBG sensors in mixed-mode delamination. J. Compos. Struct., 94(9), 2012: 2879-2887

[7] Stutz, S., Cugnoni, J., Botsis, J.. Studies of mode I delamination in monotonic and fatigue loading using FBG wavelength multiplexing and numerical analysis. Compos. Sci. Technol., 71(4), 2011: 443-449

[8] Lucas F.M. da Silva, P.M.G.P. Moreira & A.L.D. Loureiro. Determination of the strain distribution in adhesive joints using Fiber Bragg Grating (FBG), Journal of Adhesion Science and Technology, 28, 2014: 14-15.

[9] Yashiro S, Wada J and Sakaida Y. A monitoring technique for disbond area in carbon fiber–reinforced polymer bonded joints using embedded fiber Bragg grating sensors: Development and experimental validation Structural Health Monitoring, 16(2), 2017: 185–201

[10] Sanderson, A. R., Ogin, S. L., Crocombe, A. D., Gower, M. R. L., Lee, R. J. Use of a surface-mounted chirped fibre Bragg grating sensor to monitor delamination growth in a double-cantilever beam test. Compos. Sci. Technol., 72(10), 2012: 1121-1126

[11] Capell, T.F, Palaniappan, J., Ogin, S. L., Crocombe, A.D., Reed, G.T., Thorne, A.M., Mohanty, L., Tjin, S.C. The use of an embedded chirped fibre Bragg grating sensor to monitor disbond

initiation and growth in adhesively bonded composite/metal single lap jointsJ Optics A – Pure and Applied Optics, 9-6, 2007: 40-44

[12] Palaniappan, J., Wang, H., Ogin, S. L., Thorne, A. M., Reed, G.T. Crocombe, A.D., Mohanty, L., Rech, Y., Tjin, S.C. Changes in the reflected spectra of embedded chirped fibre Bragg gratings used to monitor disbonding in bonded composite joints. Comp Sci and Tech, 67, 2007: 2487-2853

[13] Murayama H, Kageyama K, Uzawa K, Ohara K and Igawa H. Strain monitoring of a single-lap joint with embedded fiber-optic distributed sensors. Structural Health Monitoring, 11(3), 2011: 325–344

[14] Ning X, Murayama H, Kageyama K, Wada D, Kanai M, Ohsawa I and Igawa H. Dynamic strain distribution measurement and crack detection of an adhesive-bonded single-lap joint under cyclic loading using embedded FBG Smart Mater. Struct. , 23, 2014: 105011

[15] Hideaki MURAYAMA, Daichi WADA, and Hirotaka IGAWA, Structural Health Monitoring by Using Fiber-Optic Distributed Strain Sensors with High Spatial Resolution. Photonic Sensors, 3(4), 2013: 355–376

[16] K. Y. Song, Z. He, and K. Hotate, "Distributed strain measurement with millimeter-order spatial resolution based on Brillouin optical correlation domain analysis," Optics Letters, 31(17), 2006: 2526–2528

[17] Güemes, A., Fernandez-Lopez, A., Soller, B. Optical Fiber Distributed Sensing - Physical Principles and Applications. Struct. Health Monitor. 9(3), 2010: 233–45.

[18] Lomperski, S., Gerardi, C., Pointer, W. D. Fiber optic distributed temperature sensor mapping of a jet-mixing flow field. Exp. Fluids. 56, 2015:1-16.

[19] Frövel, M., Del Olmo, E., Fernández, A., Quero, F., Carrión, G., Pintado, J.M., Güemes, A. Damage detection by load path changes in reinforced composite panels using local FBGs and distributed sensing. 6th European Workshop on Structural Health Monitoring (2012).

[20] Grave, J.H.L., Håheim, M.L., Echtermeyer, A.T. Measuring Changing strain fields in composites with Distributed Fiber-Optic Sensing using the optical backscatter reflectometer. Composites Part B, 74, 2015: 138-146

[21] Grave JHL, Echtermeyer AT, Strain fields in adhesively bonded patch repairs of damaged Metallic beams, Polymer Testing, 48, 2015: 50-58

[22] Andrea Bernasconi, Md Kharshiduzzaman & Lorenzo Comolli Strain Profile Measurement for Structural Health Monitoring of Woven Carbon-fiber Reinforced Polymer Composite Bonded joints by Fiber Optic Sensing Using an Optical Backscatter Reflectometer, The Journal of Adhesion, 92 (6), 2016: 440-458,

[23] Bernasconi A., Carboni M., Comolli L., Galeazzi R., Gianneo A., Kharshiduzzaman M. Fatigue crack growth monitoring in composite bonded lap joints by a distributed fibre optic sensing system and comparison with ultrasonic testing. The Journal of Adhesion, 92(7-9), 2016: 739-757.

[24] Wong, L.; Chowdhury, N.; Wang, J.; Chiu, W.K.; Kodikara, J. Fatigue Damage Monitoring of a Composite Step Lap Joint Using Distributed Optical Fibre Sensors. Materials, 9, 2016: 374-385.

[25] Hongzhuang Zhang, Changyou Li, Weibing Dai, Yuzhuo Liu, Sen Tian, Wenchao Huang, Dawei Jia, David He, Yimin Zhang, Static compression testing CFRP single-lap composited joints using X-ray μCT, Composite Structures, 234, 2020: 111667.

[26] V. Dumont, C. Badulescu, G. Stamoulis, J. Adrien, E. Maire, A. Lefèvre & D. Thévenet (2020) On the effect of the curing cycle on the creation of pores in structural adhesive joints by means of X-ray microtomography, The Journal of Adhesion, DOI: 10.1080/00218464.2020.1728257

[27] V. Dumont, C. Badulescu, J. Adrien, N. Carrere, D. Thévenet & E. Maire (2019) Experimental investigation of porosities evolution in a bonded assembly by means of X-ray tomography, The Journal of Adhesion, DOI: 10.1080/00218464.2019.1685984

[28] V. Dumont, C. Badulescu, G. Stamoulis, J. Adrien, E. Maire, A. Lefèvre, D. Thévenet. On the influence of mechanical loadings on the porosities of structural epoxy adhesives joints by means of in-situ X-ray microtomography, International Journal of Adhesion and Adhesives, 99, 2020: 102568,

[29] M. Lißner, E. Alabort, H. Cui, R. Rito, B.R.K. Blackman, N. Petrinic, Experimental characterisation and numerical modelling of the influence of bondline thickness, loading rate,

and deformation mode on the response of ductile adhesive interfaces, Journal of the Mechanics and Physics of Solids, 130, 2019: 349-369

[30] Jidong Kang, Yuhua Chen, David Sigler, Blair Carlson, David S. Wilkinson, Effect of adhesive on fatigue property of Aural2 to AA5754 dissimilar aluminum alloy resistance spot welds, Engineering Failure Analysis, 69, 2016: 57-65

[31] R.S. Choudhry, Syed F. Hassan, S. Li, R. Day, Damage in single lap joints of woven fabric reinforced polymeric composites subjected to transverse impact loading, International Journal of Impact Engineering, 80, 2015: 76-93

[32] Sheriff O. Olajide, Benedicta D. Arhatari, Recent progress on damage mechanisms in polymeric adhesively bonded high-performance composite joints under fatigue, International Journal of Fatigue, 95, 2017: 45-63,

[33] Quaresimin M., Ricotta M., "Fatigue behaviour and damage evolution of single lap bonded joints in composite material", Comp Sci Technol, 66(2), 2006: 176-187.

[34] A. Bernasconi, S. Beretta, F. Moroni & A. Pirondi. Local Stress Analysis of the Fatigue Behaviour of Adhesively Bonded Thick Composite Laminates, The Journal of Adhesion, 86:5-6, 2010, 480-500,

[35] ISO 25217:2009, Adhesives — Determination of the mode 1 adhesive fracture energy of structural adhesive joints using double cantilever beam and tapered double cantilever beam specimens, Geneva, 2009

[36] Optical Distributed Sensor Interrogator Model ODiSI-B: User's Guide ODiSI-B Software 5.2.0 2017 Luna 3155 State Street Blacksburg, VA 24060.

[37] Kharshiduzzaman, M., Gianneo, A., Bernasconi, A. Experimental analysis of the response of fiber Bragg grating sensors under non-uniform strain field in a twill woven composite (2019) Journal of Composite Materials 53(7), pp. 893-908